AIAA JOURNAL
Vol. 42, No. 2, February 2004

Near-Surface Topology and Flow Structure on a Delta Wing

M. M. Yavuz,* M. Elkhoury,† and D. Rockwell‡
Lehigh University, Bethlehem, Pennsylvania 18015

The streamlines, and the corresponding patterns of velocity and vorticity, are characterized on a plane immediately adjacent to the surface of a delta wing using a laser-based technique of high-image-density particle image velocimetry. This technique provides the sequence of instantaneous states, as well as the corresponding time-averaged state, of the near-surface streamline topology and the associated critical points. These topological features are interpreted in terms of patterns of averaged and unsteady velocity, and averaged vorticity, which allow identification of regions of unsteadiness along the surface of the wing. These representations of the flow patterns on the stationary wing are also employed for the case of the wing subjected to small-amplitude perturbations in the pitching mode. Perturbations at or near the inherent frequency of the predominant unsteady event on the stationary wing yield substantial changes of the surface topology and flow structure. Furthermore, response of this topology and flow structure to transient, ramplike pitching motion is addressed to define the succession of states during the relaxation process immediately after cessation of the wing motion.

I. Introduction

THE focus of the present investigation is on the surface topology of stationary and perturbed delta wings having a low sweep angle. Previous related investigations include experimental and numerical studies of the flow structure above wings of low and moderate sweep angle and investigations of surface topology for not only delta wings, but also a wide range of aerodynamic and wind engineering configurations. These previous related studies are included in the summaries that follow.

A. Flow Structure Above Delta Wings of Low and Moderate Sweep Angle

Delta wings having low and moderate values of sweep angle, which represent generic features of unmanned combat air vehicle (UCAV) configurations, can give rise to distinctive types of flow structure. This has been the subject of recent investigations. Ol and Gharib[1] employed a stereo version of particle image velocimetry to characterize the three-dimensional structure on crossflow planes of wings of sweep angle $\Lambda = 50$ and 65 deg. Gursul et al.[2] used a dye technique, along with complementary particle image velocimetry on crossflow planes, to visualize the vortex cores on wings of various planforms having low sweep angle. Yaniktepe and Rockwell[3] employed a cinema technique of particle image velocimetry to characterize the crossflow streamline topology, Reynolds stress, and spectra of velocity fluctuations in relation to instantaneous patterns of the flow structure, for a range of angles of attack of a wing having a low sweep angle $\Lambda = 38.7$ deg. Gordnier and Visbal[4] provided the first numerical simulations of the instantaneous flow structure on a wing of moderate sweep angle $\Lambda = 50$ deg. An in-depth assessment of the relationship between the instantaneous and averaged structure of leading-edge vortices is provided by Visbal and Gordnier,[5] who originate high-resolution numerical simulations and corresponding interpretations for the case of a wing having relatively high sweep angle $\Lambda = 75$ deg; the concepts of the advance, including the existence of time-averaged substructures in transitional/turbulent shear layers from the leading edge, are equally applicable to wings of low to moderate sweep angle of interest herein.

B. Surface Flow Topology

Over the past few decades, a wide range of investigations, primarily in the area of aerodynamics, have addressed the surface topology on three-dimensional and planar surfaces, including the simplified planform of a delta wing, by the use of both numerical and experimental approaches. Representative investigations are described in the overviews of Hunt et al.,[6] Moffat and Tsinober,[7] Tobak and Peake,[8] Peake and Tobak,[9,10] and Lazos.[11] The focus of the present study is on the surface topology of delta wings having low sweep angle Λ; very few investigations have been performed. Su et al.[12] deduced the time-averaged shear stress lines with an oil film technique for delta wings with $\Lambda = 30$ and 45 deg. Gordnier and Visbal[4] numerically computed the surface streamlines on a delta wing of $\Lambda = 50$ deg in relation to the flow patterns above the wing surface.

From a conceptual standpoint, topological interpretations based on critical point theory have been used in a diverse series of investigations of flow past aerodynamic surfaces and wind engineering configurations. A critical point is defined to occur in the flowfield at a location where the slope of the streamline is indeterminate and the velocity is zero; examples of critical points include foci, nodes, and saddle points. Experimental studies have employed time-averaged surface visualization, by the use of an oil film approach or its equivalent, which allows definition of the surface shear stress lines, and their interpretation via critical point theory, as described, for example, by Perry and Fairly[13] and Tobak and Peake.[8] The relationship of surface shear stress lines to surface streamlines was addressed theoretically by Squire[14] and Lighthill.[15] Hunt et al.[6] specified the criteria for similarity of patterns of critical points of the surface shear stress and velocity fields. On the basis of these criteria, and as suggested by Lighthill,[15] the shear stress lines may also be designated as surface streamlines. The aim of the present investigation is not, however, to establish a means for determination of the shear stress lines via the surface streamlines. Rather, it is to provide a means for characterizing the footprint of the unsteady and averaged flow structure at a reference elevation immediately adjacent to the surface of the wing and the manner in which this structure is altered by the motion of the wing. Herein, all references to surface quantities, such as surface topology, are to be interpreted as on a plane adjacent to the surface, i.e., near-surface topology.

C. Unresolved Issues

From an experimental standpoint, the traditional method of determining the near-surface patterns of aerodynamic configurations is oil film visualization of shear stress lines. Such visualization yields

Received 1 July 2003; revision received 30 September 2003; accepted for publication 8 October 2003. Copyright © 2003 by the authors. Published by the American Institute of Aeronautics and Astronautics, Inc., with permission. Copies of this paper may be made for personal or internal use, on condition that the copier pay the $10.00 per-copy fee to the Copyright Clearance Center, Inc., 222 Rosewood Drive, Danvers, MA 01923; include the code 0001-1452/04 $10.00 in correspondence with the CCC.

*Research Assistant, Department of Mechanical Engineering and Mechanics.
†Research Assistant, Department of Mechanical Engineering and Mechanics. Student Member AIAA.
‡Paul B. Reinhold Professor, Department of Mechanical Engineering and Mechanics; dor0@lehigh.edu. Member AIAA.

time-averaged patterns that have provided valuable insight and guidance. Not yet addressed are the possible instantaneous patterns of surface topology and the associated critical points that contribute to the time-averaged representations. Furthermore, the relation of these possible topological states to surface vorticity and velocity, including fluctuation amplitudes of these quantities, has not been pursued, despite the potential for new types of interpretations of surface buffeting due to vortex breakdown, as well as the onset of localized, three-dimensional stall.

In addition to issues associated with this class of experimental approaches, there are a number of central, specific points related to quantitative flow patterns on wings of small sweep angle at sufficiently high angle of attack, such that vortex breakdown and localized stall occur on the wing surface. These points include the following:

1) Dye or smoke visualization can provide valuable insight into the development of leading-edge vortices on wings of low sweep angle. Quantitative patterns extending over the entire surface of the wing could, however, provide insight into regions beneath the onset of vortex breakdown, as well as areas corresponding to the onset of three-dimensional separation and stall that define the distinctive features of flow past wings having low sweep. Such patterns have not yet been pursued.

2) The quantitative patterns of the streamline topology, as well as other features of the flow structure on the surface of the wing, may be related to the structure of the wake of the wing. In other words, the degree to which the topology on the surface of the wing extends into the wake region, especially for wings of low sweep angle, has not been pursued in terms of instantaneous and time-averaged patterns.

3) The potential for control of the surface topology and flow structure via small-amplitude perturbations of the wing, and the manner in which they are transformed from those of the stationary wing described in item 1 has not yet been addressed. The issue arises as to whether it is possible to mitigate regions of localized separation and stall while radical alterations of the surface topology and critical points are induced.

4) The nature of the topological states during relaxation from an imposed ramplike pitching motion of the wing, by the use of the quantitative approaches of item 1, has not been addressed.

The overall aim of the present investigation is to pursue the aforementioned patterns on the surface of the wing, as well as the patterns of separated flow in the vicinity of the leading and trailing edges and the manner in which they respond to controlled motion of the wing. In doing so, a technique of high image density particle image velocimetry will be employed.

II. Experimental System and Techniques

Experiments were performed in a large-scale water channel, which had a test section of 927-mm width, 610-mm depth, and 4928-mm length. The freestream turbulence intensity at the entrance to this section was less than 0.1%. The walls of this section were optically transparent. The free surface of the water was maintained at a height of 559 mm. All experiments were performed at a freestream velocity of $U = 98.8$ mm/s, and the Reynolds number based on the chord of the delta wing was $Re = 1 \times 10^4$.

The delta wing had a sweep angle of $\Lambda = 38.7$ deg. The chord C was 101.6 mm, and the total span at the trailing edge was 254 mm. The thickness of the wing was 9.53 mm, and its leading edges were beveled on the windward side at an angle of 15 deg. The angle of attack of the wing was maintained at $\alpha = 10$ deg.

The delta wing was held in position by a 6-mm-diam sting that had a length of 150 mm. It had the form of a classical sting attached to the trailing edge of the wing, that is, it extended normal to the surface of the trailing edge of the wing, which was aligned with the plane of symmetry of the wing. This sting was connected to a U-shaped support frame, then to a motor drive mechanism above the water surface that imparted static and dynamic variations of angle of attack, around the midchord, without interfering with the flow along the delta wing.

A technique of high image density particle image velocimetry was employed to generate quantitative flow patterns. The flow was seeded with 12-μm metallic-coated hollow plastic spheres that had a specific gravity of 1.03. The seeding density of these particles was sufficiently large to satisfy the criterion of high image density. Illumination was provided by a dual-pulsed 90 mJ Nd:Yag laser system, which was located below the water channel. The time difference between pulses of the dual laser system was 10 ms. The laser sheet of desired thickness, focal distance, and orientation was generated by transmitting the laser beam through an optical train involving a prism, two -15-mm cylindrical lenses, and 500-mm spherical lens.

For acquisition of images, a digital charge-coupled device (CCD) camera was used to record the patterns of particle images. The camera had a total of 1024×1024 pixels, of which 1008×1016 were light sensitive, and it was equipped with a lens of focal length 60 mm, thereby providing a magnification of 1:3.62. The field of view was 252×260 mm. The camera was used at its maximum framing rate of 30 frames/s, which gave 15 sets of images per second. In the image layouts that follow, N is frame number. The difference $N_2 - N_1$ between two successive values of N of the image sequence at 15 Hz corresponds to a dimensionless time $(t_2 - t_1)U/C = 0.065$, in which U is the freestream velocity and C is the wing chord.

A frame-to-frame cross-correlation technique was employed to determine the velocity field. The effective size of the interrogation window was 32×32 pixels. To satisfy the Nyquist criterion, an overlap of 50% was employed during the interrogation process. This approach yielded a total of 58×60 (3480) velocity vectors. The effective grid size was 4.44 mm in the plane of the laser sheet. The smallest-scale vortical structure that can be resolved is between one and two times the distance between grid points.

For acquiring dye images, dye was injected near the tip of the wing apex, and the same CCD camera was used as before.

To characterize the near-surface topology of the flow, the laser sheet was located parallel, and immediately adjacent to, the surface of the wing, as indicated in the plan and side views of Fig. 1. For all images shown herein, the laser sheet had a thickness of 1 mm. The center of the sheet was located a distance of 1 mm from the surface of the wing. This distance corresponds to a displacement z normal to the surface of the wing of $z/C = 0.01$, in which C is the root chord. At this value of dimensionless elevation z/C, the time-averaged streamlines may be viewed as averaged representations over the 1-mm-thick layer corresponding to the laser sheet. They will be

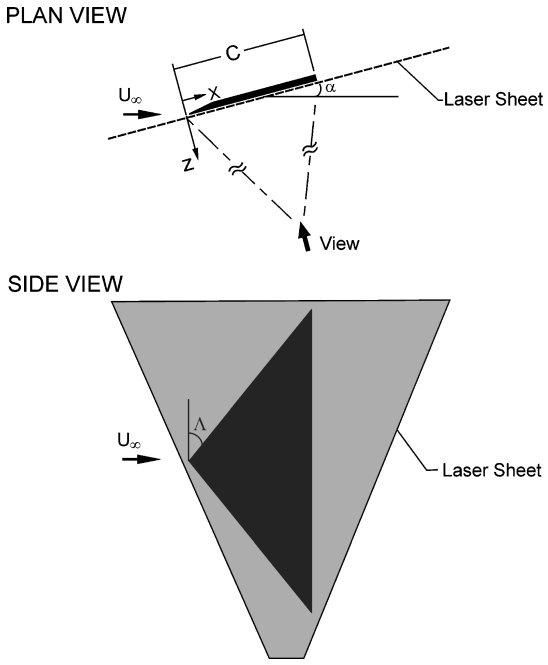

Fig. 1 Overview of delta wing and laser sheet orientation for quantitative imaging.

referred to herein as near-surface streamlines, that is, streamlines immediately adjacent to the surface of the wing; their interpretation as surface shear stress lines, however, is not appropriate because the equivalency conditions of Hunt et al.[6] have not yet been assessed. For this layer, defined by the laser sheet, and at the angle of attack employed herein, the time-averaged patterns of velocity, streamline topology, and vorticity normal to the surface of the wing were found to be relatively insensitive to small variations of z/C. In fact, at values of $z/C = 0.005$, 0.015, and 0.02, these patterns showed insignificant deviation from those at $z/C = 0.01$, whereas at higher elevations, significant departures were evident.

Both instantaneous and averaged images are considered herein. Unless otherwise indicated, an averaged image was determined from 200 images acquired at a rate of 15 Hz, the framing rate of the camera. When small amplitude ($\Delta\alpha = 1$ deg) pitching perturbations were applied according to $\alpha(t) = \bar{\alpha} + \Delta\alpha \sin \omega_e t$, in which $\bar{\alpha}$ is a steady angle of attack, the averaged image was calculated from the images at $\bar{\alpha}$ for successive upstroke and downstroke motions of the wing. This constraint is necessary because the distance from the surface of the wing to the laser sheet changes during the oscillation cycle, and only at $\bar{\alpha}$ is this distance constant along the chord of the wing, thereby allowing a valid comparison with the patterns of the stationary wing. To determine the rate of convergence of the time-averaged patterns of velocity and streamline topology for the perturbed wing, 6, 12, 20, and 80 images were averaged at $T_e = 0.31$ s. The patterns were nearly indistinguishable for averages of 6 and 80 images, no doubt due to the tendency for the perturbation to promote organized structure. Further tests for the rate of convergence for other values of T_e employed in this investigation showed that an averaged image based on 20 instantaneous images was also a conservative criterion; it was, therefore, employed for all imaging.

The location of the wing boundary was determined, first, from the raw image files of the quantitative images, which positioned the leading edge of the wing with an uncertainty of sweep angle of ± 0.5 deg. The final, precise location was then determined with the aid of constant contours of averaged vorticity, such that extrema of vorticity in the vicinity of the leading edge were compatible with both the locus of the edge as well as the bifurcation lines of the averaged streamwise velocity.

III. Surface Topology of Stationary Wing

Figure 2 shows, in the top-left-hand image, the time-averaged surface streamlines for the present wing. For comparison, the top-right-hand image shows time-averaged patterns of surface shear stress lines on a delta wing of low sweep angle from Ref. 12. This image was acquired in a wind tunnel by the use of an oil film technique, whereby time-averaged patterns were allowed to form over a sufficiently long time interval. The present pattern shows a remarkable similarity to the oil film pattern. Saddle points, which correspond to apparent intersections of surface streamlines and surface shear stress lines, and are designated as S, occur near the leading edge of both wing configurations. Also, the nodal points N in the present image, appear near the leading edge, at a location slightly downstream of the apex, which matches with the point designated on the oil film image. Whereas saddle points S require knowledge of the three-dimensional flow to classify them as either separation or attachment saddles, such a classification can be attained for nodes N on the basis of two-dimensional patterns. The nodes N indicated in the upper-left-hand image of Fig. 2 are nodes of separation because the streamlines are oriented toward the node. A node of attachment would, therefore, correspond to streamlines oriented away from the node. This same interpretation can be applied to all nodes designated in the topological patterns subsequently.

Nodal points on the oil film pattern, however, cannot be identified conclusively due to resolution issues. Furthermore, note that the large-scale swirl patterns of the present image are in accord with those of the oil film image. These swirl patterns occur inboard of the saddle points. These features of the surface topology are fundamentally different than those on a wing of relatively high sweep, as is evident in comparisons with Ref. 12.

Another feature of Fig. 2 is that the streamline pattern on the surface of the wing is compatible with that formed in the near wake of the wing, that is, the surface streamlines of the present configuration, shown in the top-left-hand image of Fig. 2, continue into the near-wake region, then swirl back toward the leading edge. This observation emphasizes that the overall pattern of time-averaged streamlines is globally compatible with both the surface of the wing and its extension into the near-wake region.

The relationship between time-averaged patterns of vorticity $\langle\omega\rangle$ and streamline topology $\langle\Psi\rangle$ is given in the bottom image of Fig. 2. It is evident that the bifurcation line of the streamline topology corresponds to the downstream edge of the elongated pattern of vorticity, which is oriented parallel to the leading edge of the wing. In fact, the lowest level of vorticity contour defined for this image is congruent with the bifurcation line. These vorticity patterns have high spatial gradients and contain small-scale extrema of vorticity.

A. Comparison of Patterns of Surface Topology and Flow Structure

Figure 3 compares various types of surface patterns. The pattern of velocity vectors $\langle \boldsymbol{V} \rangle$ shown in the top-left-hand image indicates that the velocity vectors have a relatively large amplitude in the central portion of the wing; however, farther outboard from the plane of symmetry, and immediately downstream of the leading edge, the magnitude of velocity becomes relatively small. The corresponding image of time-averaged streamlines $\langle\Psi\rangle$, shown at the top right of Fig. 3, indicate the presence of saddle points d and nodal points b already designated in Fig. 2. In addition, the negative bifurcation line c of the streamline pattern, which corresponds to the confluence of streamlines from the freestream and streamlines representing the large-scale swirl pattern, are oriented toward the apex of the wing.

Further interpretation of the time-averaged pattern of velocity is provided by contours of constant streamwise velocity $\langle u\rangle/U$ given in the middle image of Fig. 3. An extremum of positive $\langle u\rangle/U$ occurs slightly downstream of apex of the wing. The shaded regions, which represent regions of negative $\langle u\rangle/U$, occur in the outboard regions. Such negative regions are associated with the large-scale swirl patterns of streamlines $\langle\Psi\rangle$.

A further representation of the surface pattern is provided by time-averaged vorticity $\langle\omega\rangle$, shown in the right-hand image in the middle of Fig. 3. Contours of solid and dashed lines represent, respectively, positive and negative $\langle\omega\rangle$, in which the positive orientation corresponds to the outward normal of the wing surface. As indicated by these patterns, only the central portion of the wing, at a location sufficiently downstream of the apex, is essentially vorticity free. The large-scale swirl patterns of the streamlines shown in the $\langle\Psi\rangle$ image generally correspond to significant values of $\langle\omega\rangle$. Local extrema of $\langle\omega\rangle$, designated as b, are located close to the shaded regions of negative $\langle u\rangle/U$. The highest values of $\langle\omega\rangle$, however, occur immediately downstream of the apex of the wing and are designated as c. These high levels of vorticity in the apex region of the wing are not associated with a focus, that is, a region of tightly wound, spiral-like streamlines, in the $\langle\Psi\rangle$ image of Fig. 3.

An additional feature of the pattern of $\langle\omega\rangle$ of Fig. 3 is the occurrence of relatively high levels at a location immediately upstream of the leading edge of the wing. In fact, these regions of $\langle\omega\rangle$ show well-defined concentrations of like sign along the leading edge, which indicate the existence of a corotating pattern of small-scale vorticity concentrations. The peak vorticity level at location a is $\langle\omega\rangle C/U = 6.17$, compared with the corresponding value of 9.26 at location c.

There are two possible interpretations of the averaged patterns of Fig. 3. The first is the occurrence of time-averaged substructures along the leading edge, first shown in the numerical simulation of Visbal and Gordnier.[5] In their interpretation, these substructures arise from averaging the flow associated with nonlinear transition of the shear layer separating from the leading edge. The second interpretation is provided by Riley and Lowson,[16] based on an investigation of a highly swept delta wing. They indicate that these structures are laminar and steady and arise from an inflectional instability of crossflow boundary layer on the windward

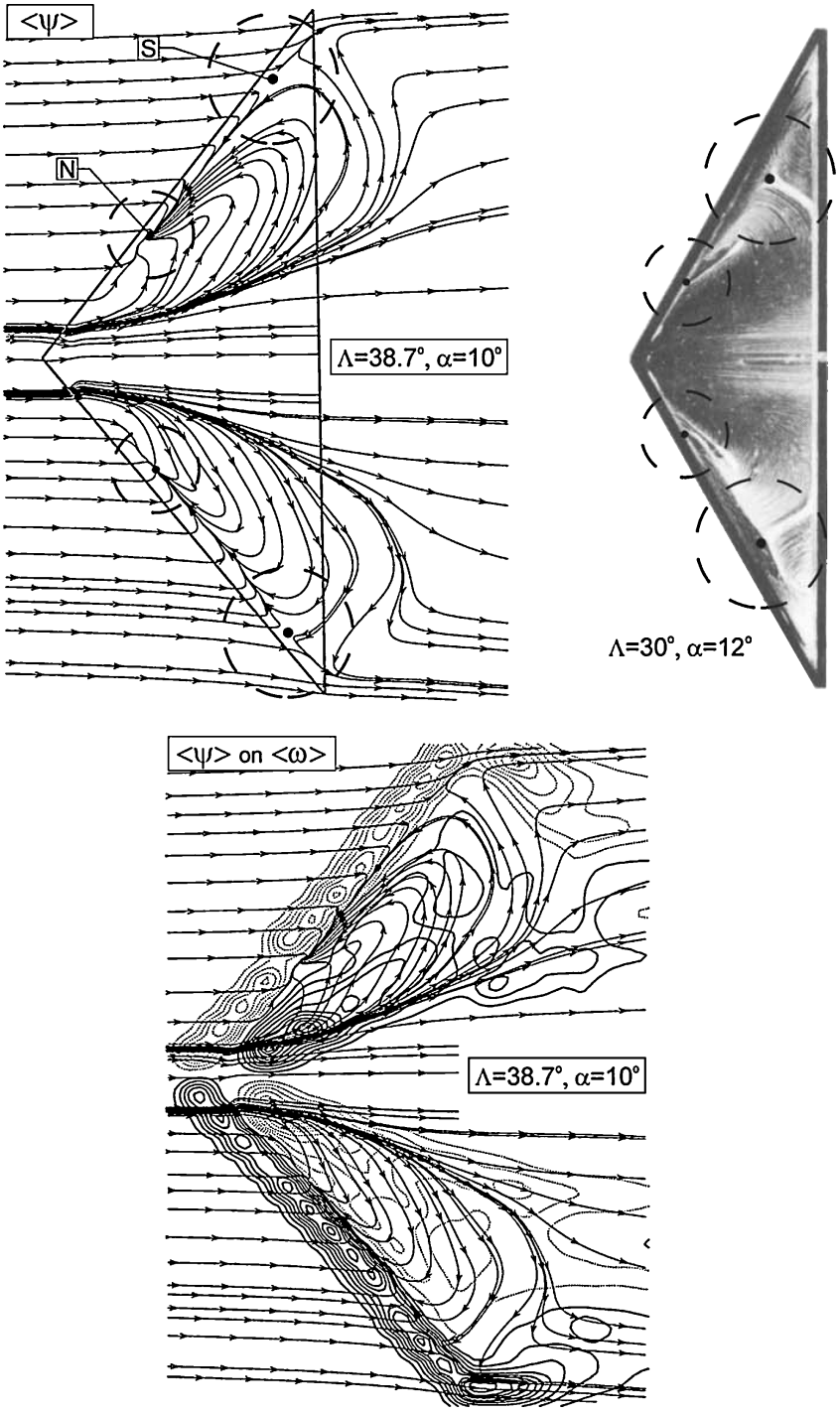

Fig. 2 Patterns of time-averaged surface streamlines $\langle\Psi\rangle$ in comparison with surface (oil film) visualization for wings of low sweep angle; superposition of pattern of averaged surface streamlines $\langle\Psi\rangle$ and averaged vorticity $\langle\omega\rangle$ oriented normal to the wing surface are also shown, and, for vorticity, minimum and incremental values are $[|\langle\omega\rangle|]_{\min} = 1\ s^{-1}$ and $\Delta[|\langle\omega\rangle|] = 1\ s^{-1}$.

side of the wing. A representative instantaneous image of vorticity ω (not shown herein) employed to determine the averaged image of $\langle\omega\rangle$ of Fig. 3 indicates distinguishable small-scale concentrations; yet the patterns of root-mean-square velocity $v_{\rm rms}/U$ given in Fig. 3, to be described, indicate that substantial fluctuations occur in this leading-edge region. The physical origin of the ordered patterns of $\langle\omega\rangle$ is, at this point, inconclusive and requires further assessment.

Unsteadiness of the leading-edge vortices is represented by the onset of undulations and an increase in cross-sectional area of the patterns of dye shown in the image at the bottom left of Fig. 3. The dye markers show the onset of pronounced, small-scale undulations immediately downstream of the apex and, as the trailing edge is approached, the cross section of the marker pattern abruptly widens. This type of structure contrasts with the abrupt onset of bubble or spiral modes of vortex breakdown on a highly swept wing. The present patterns of dye visualization were unsteady, and the apparent location of the abrupt widening of the marker was not stationary; rather, it oscillated back and forth in the streamwise direction. This visualization of the onset of vortex core undulations and vortex breakdown is closely linked to the contours of constant root-mean-square velocity $v_{\rm rms}/U$ given in the image at the bottom right of Fig. 3. Because of the unusual form of vortex breakdown and the aforementioned time-dependent excursions of the apparent

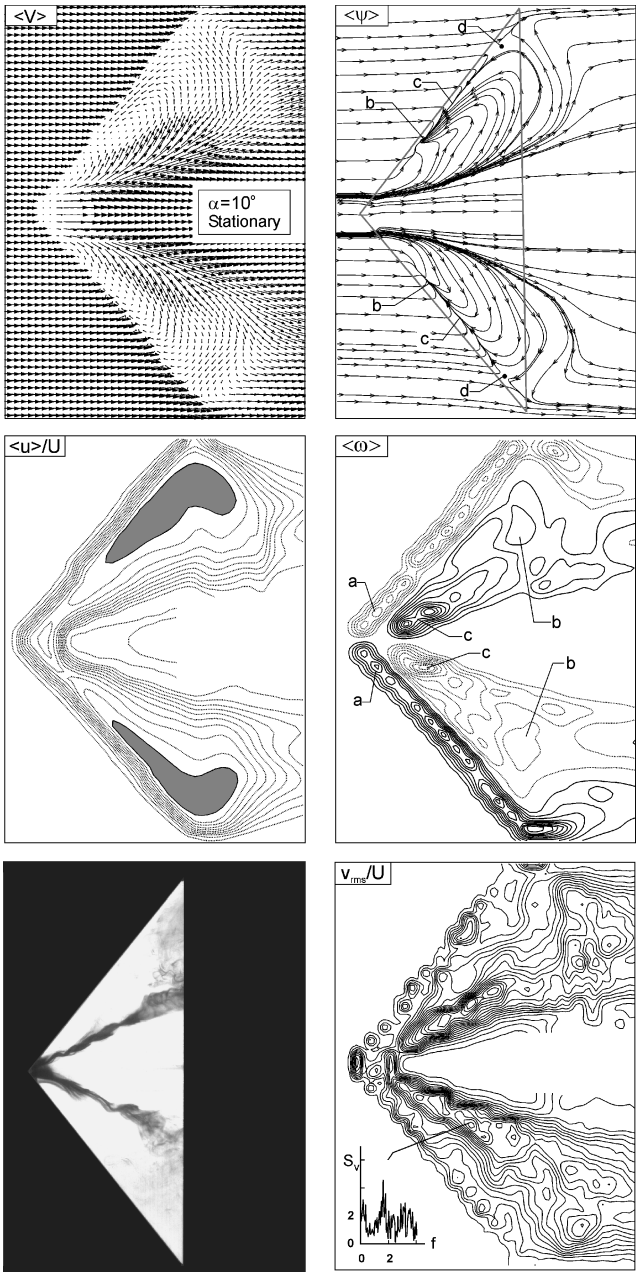

Fig. 3 Comparison of patterns of time-averaged velocity $\langle V\rangle$; streamlines $\langle\Psi\rangle$; streamwise velocity component $\langle u\rangle/U$ ($[|\langle u\rangle/U|]_{\min}=0.05$, $\Delta[|\langle u\rangle/U|]=0.1$); vorticity $\langle\omega\rangle$ ($[|\langle\omega\rangle|]_{\min}=1\ s^{-1}$, $\Delta[|\langle\omega\rangle|]=1\ s^{-1}$); root mean square of transverse velocity v_{rms}/U ($[v_{rms}/U]_{\min}=0.02$, $\Delta[v_{rms}/U]=0.01$); and dye visualization.

location of the vortex breakdown, it is difficult to relate the onset of breakdown to a reference location in either the contours of constant $v_{\rm rms}/U$ or the corresponding spectra $S_v(f)$. The largest values of $v_{\rm rms}/U$ correspond to the location beneath the unsteady, leading-edge vortex for computation of the spectrum $S_v(f)$, which is given in the inset of the image of $v_{\rm rms}/U$. This spectrum was calculated from a cinema sequence of particle image velocimetry (PIV) images, where the variation of the unsteady velocity fluctuation $v(t)$ was determined at the indicated location. A sharply defined peak occurs at $f=1.6$ Hz and a broader peak at its approximate first harmonic 3.2 Hz. The dimensionless values of these frequencies are $fC/U=1.65$ and 3.29, respectively. These values of fC/U are generally consistent with the range of frequencies corresponding to vortex breakdown, as computed for surface pressure fluctuations by Gordnier and Visbal,[4] as well as those for velocity fluctuations determined experimentally on the basis of cinema PIV imaging, at locations away from the surface, by Yaniktepe and Rockwell.[3] Both of the aforementioned investigations involved wings of relatively low sweep angle. Furthermore, these values compare with dimensionless frequencies of the order of $fC/U=$ 1–4, determined from pointwise surface pressure and velocity measurements within the unsteady vortex on a highly swept wing by Menke et al.[17]

B. Relation of Time-Averaged Topology to Instantaneous Topology

The patterns of the flow structure shown in Fig. 3 are all time-averaged representations, which, of course, are due to a sequence of instantaneous states. A comparison of the time-averaged topology of the surface streamlines is compared with representative instantaneous patterns in Fig. 4. The instantaneous patterns were randomly selected to point out features that were both symmetrical and asymmetrical with respect to the plane of symmetry of the wing. In all instantaneous images, the saddle point at location d is clearly identifiable, and one concludes that it is a persistent, dominant feature of both the instantaneous and time-averaged topologies. Likewise, the bifurcation line adjacent to the leading edge of the wing, c, is also a very consistent feature, as is the nodal point b. An important, distinguishing feature of the instantaneous patterns is, however, the occurrence of well-defined foci, which represent regions of spiral streamline patterns designated as a. In some cases, a bifurcation line integrated with a focus (images $N=93$ and 181, Fig. 4) is apparent, instead of a distinctly separate bifurcation line and focus. In image $N=93$, the foci a tend to appear at the same chordwise location on either side of the plane of symmetry, whereas in image $N=148$, a focus a is apparent only on the starboard side of the wing, and in image $N=181$, these foci a occur relatively close to the apex of the wing (Fig. 4). Because of the highly nonstationary nature of the foci a, which involve large variations in spatial location along the surface of the wing in successive instantaneous images Ψ, as well as intermittent lack of symmetry on either side of the wing, the time-averaged consequence is a pattern

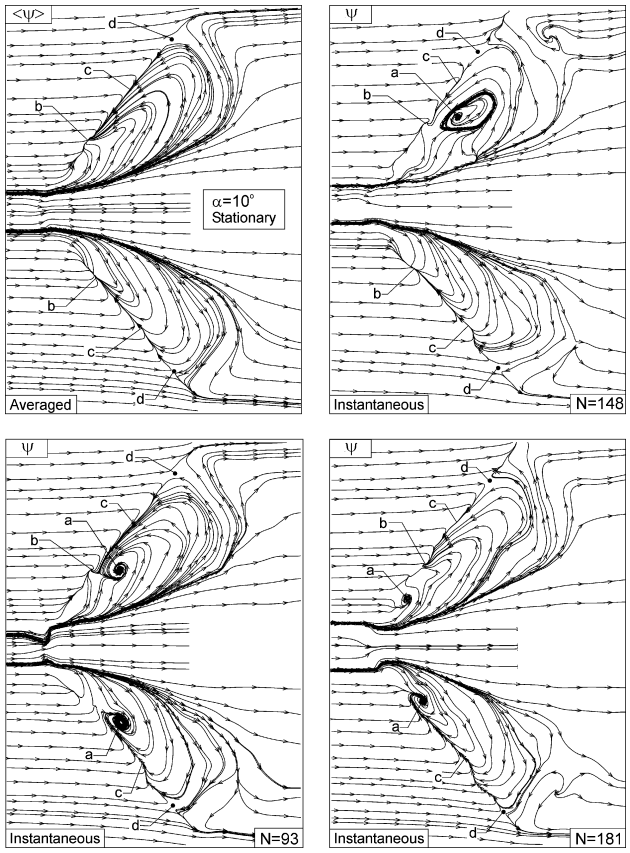

Fig. 4 Patterns of time-averaged $\langle\Psi\rangle$ and instantaneous Ψ streamline topology for various frame numbers N of cinema sequence and angle of attack $\alpha=10$ deg.

of streamline topology without clearly defined foci, as evident in the $\langle\Psi\rangle$ image of Fig. 4.

IV. Effect of Wing Perturbations on Flow Structure

The consequence of small amplitude sinusoidal perturbations of angle of attack according to $\alpha(t) = \bar{\alpha} + \Delta\alpha \sin \omega_e t$ is shown in the dye visualization of Fig. 5. The values of nominal and perturbation angles of attack are $\bar{\alpha} = 10$ deg and $\Delta\alpha = 1$ deg. The period of excitation, which is given in each of the images of Fig. 5 as $T_e = 0.31$, 0.75, and 1 s, was selected to incorporate the range of naturally occurring spectral peaks in the region of vortex breakdown, as shown in the lower-right-hand image of Fig. 3. For these values of T_e, the corresponding values of perturbation frequency are $f_e = 3.23$, 1.33, and 1 Hz, which cover the spectral peaks at $f = 1.6$ and 3.2 Hz in the spectrum of Fig. 3. The amplitude $\Delta\alpha = 1$ deg was selected to determine whether such a small displacement amplitude could significantly affect the flow structure. This value was the smallest that could be reliably attained with the computer-controlled forcing system.

Consider, first, the $T_e = 0.31$ s image of Fig. 5. Well-defined swirl undulations of the vortex core are induced, and they are evident, albeit with a small amplitude, at a location very close to the apex of the wing. The scale of these undulations increases substantially with chordwise distance along the leading edge of the wing. In $T_e = 0.75$ s image in Fig. 5 shows the pattern of dye takes when the perturbation period is increased. Swirl-type undulations are no longer evident in the region immediately downstream of the apex but eventually emerge as indicated and then lose their coherence as the trailing edge of the wing is approached. A generally similar, though less coherent, pattern of swirl-type undulation is evident at the larger $T_e = 1$ s image of Fig. 5. Thus, in essence, the onset of ordered undulations of the dye marker moves farther downstream with increasing period T_e; this effect appears to be a true feature of the flow physics. On the other hand, the change in the apparent diameter of the dye marker may well be due to the influence of the perturbation on the injection of dye from the ports; this observation is consistent with the fact that, as the period T_e becomes large, the diameter of the marker approaches that of the stationary wing. Examination of cinema sequences of the aforementioned dye patterns show that they had a very similar form and location of vortex breakdown over the entire oscillation cycle. In other words, phase referencing of the images was not necessary, apparently due to the small displacement amplitude and the sufficiently high frequency, which preclude relaxation processes of the flow. This situation contrasts with classical experiments involving highly swept wings, which involve large-amplitude pitching motion, long timescales, and, thereby, substantial excursions of the onset of vortex breakdown.

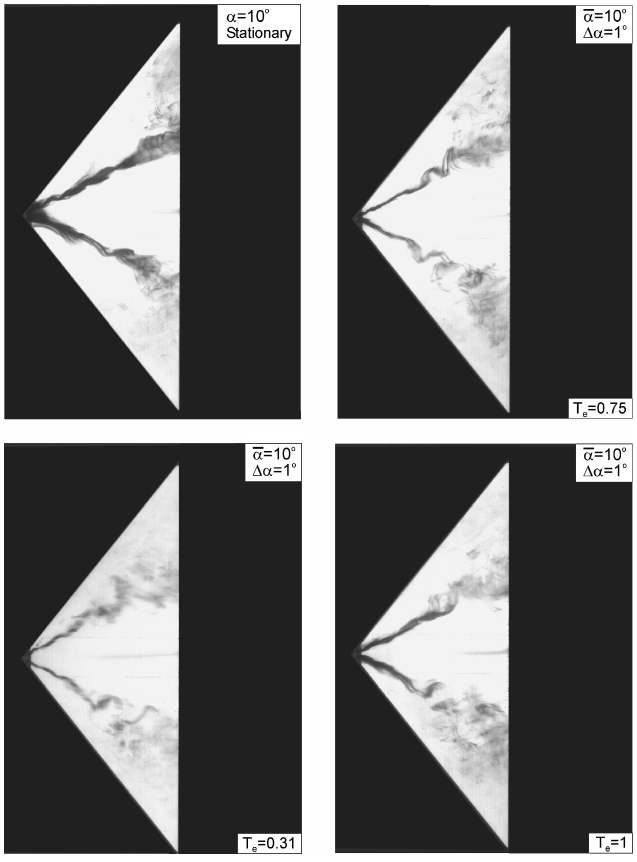

Fig. 5 Dye visualization of leading-edge vortices on a stationary wing at angle of attack $\alpha = 10$ deg and wing perturbed according to $\alpha(t) = \bar{\alpha} + \Delta\alpha \sin \omega_e t$, in which $\omega_e = 2\pi/T_e$. (T_e in seconds); unsteadiness of leading-edge vortices has a predominant period of $T_0 = 0.63$ s, therefore, values of $T_e/T_0 = 0.5$, $T_e/T_0 = 1.2$, and $T_e/T_0 = 1.6$.

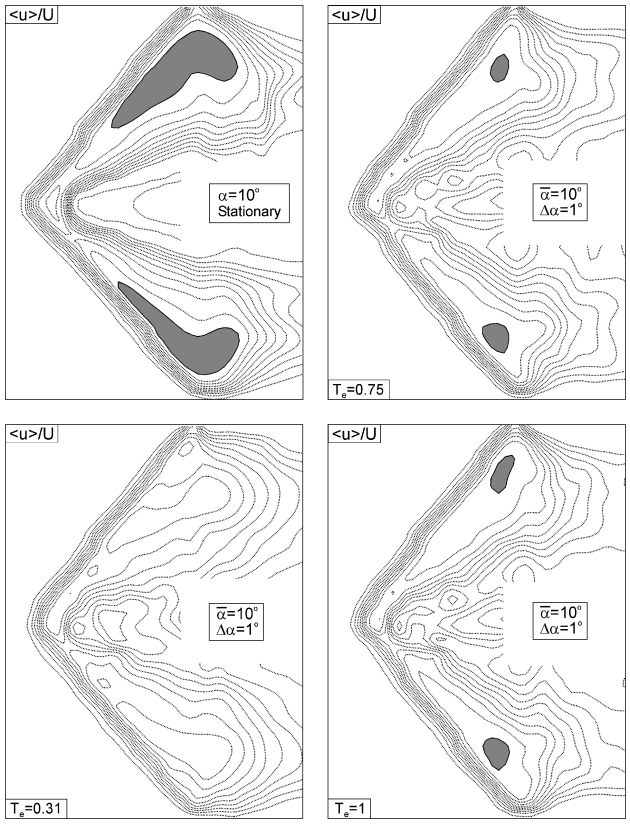

Fig. 6 Patterns of time-averaged component of streamwise velocity $\langle u\rangle/U$ on a stationary wing and the wing perturbed according to $\alpha(t) = \bar{\alpha} + \Delta\alpha \sin \omega_e t$, in which $\omega_e = 2\pi/T_e$; minimum and incremental values are $[|\langle u\rangle/U|]_{\min} = 0.05$ and $\Delta[|\langle u\rangle/U|] = 0.1$.

Figures 6–10 show averaged representations of the near-surface patterns for the perturbed wing, relative to the stationary wing. As described in detail in Sec. II, the averaged images for the perturbed wing are based on the instantaneous images at the nominal (steady) angle of attack $\bar{\alpha} = 10$ deg; the angle of attack of the corresponding stationary wing was $\alpha = 10$ deg.

Figure 6 shows the consequence of the perturbations on the contours of constant streamwise velocity $\langle u\rangle/U$, relative to the case of the stationary wing. The shaded regions represent negative values of $\langle u\rangle/U$. At $T_e = 0.31$ s, the regions of negative $\langle u\rangle/U$ are eliminated altogether, and, at larger values of $T_e = 0.75$ and 1 s, they are distinguishable, but substantially reduced in extent relative to the case of the stationary wing.

In the patterns of transverse velocity $\langle v\rangle/U$, indicated in Fig. 7, contours represented by the solid and dashed lines, respectively, represent negative and positive $\langle v\rangle/U$, in which the positive sign corresponds to the upward direction. The perturbation at $T_e = 0.31$ s results in a substantial reduction of the peak value of $\langle v\rangle/U$. In fact, this reduction is by a factor of approximately one-half. As the value

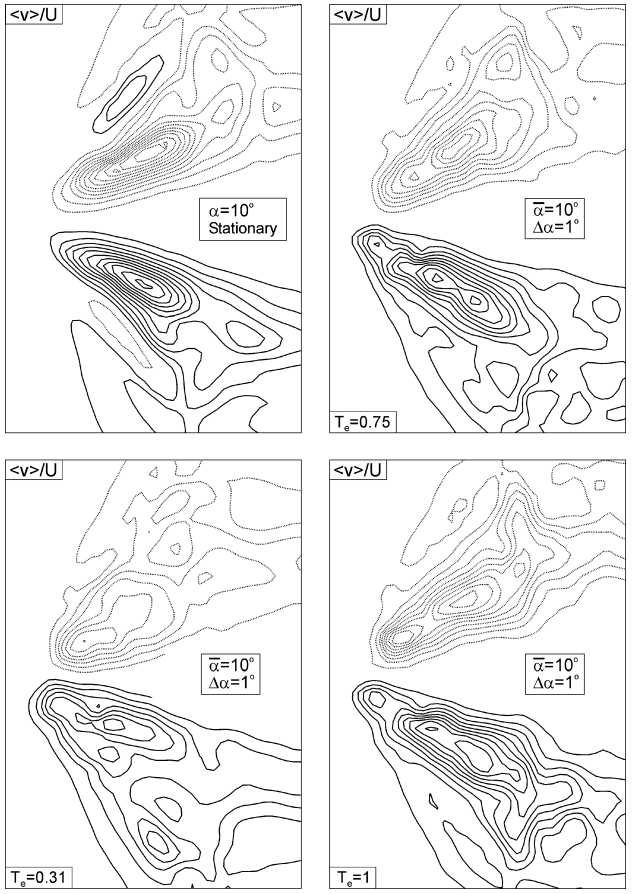

Fig. 7 Patterns of time-averaged component of transverse velocity $\langle v \rangle$ on a stationary wing at angle of attack $\alpha = 10$ deg and the wing perturbed according to $\alpha(t) = \bar{\alpha} + \Delta\alpha \sin \omega_e t$, in which $\omega_e = 2\pi/T_e$; minimum and incremental values are $[|\langle v \rangle/U|]_{\min} = 0.05$ and $\Delta[|\langle v \rangle/U|] = 0.05$.

of T_e increases to 0.75 and 1 s, the peak values of $\langle v \rangle / U$ recover toward the values for the stationary wing.

The foregoing alterations of patterns of $\langle u \rangle / U$ and $\langle v \rangle / U$ are, of course, manifested in the patterns of time-averaged streamline topology $\langle \Psi \rangle$ shown in Fig. 8. At $T_e = 0.31$ s, the spanwise extent Δ of the inflow region of the streamline patterns is significantly reduced, and, furthermore, the large-scale swirl pattern, so prevalent in the pattern of $\langle \Psi \rangle$ on the stationary wing, is no longer evident. Moreover, the direction of the bifurcation line b at $T_e = 0.31$ s is actually reversed, relative to that on the stationary wing. This reversal is actually discernible in representative instantaneous images (not shown). At larger values of $T_e = 0.75$ s, the same observations hold, though the details of the streamline pattern are altered. For example, the pattern at T_e has an overall form that is closer to the swirl pattern on the stationary wing, relative to the form on the wing perturbed at $T_e = 0.31$ s. For all perturbed cases, note that the saddle and nodal points no longer exist.

Corresponding patterns of averaged vorticity $\langle \omega \rangle$ are given in Fig. 9. At $T_e = 0.31$ s, the peak value of vorticity $\langle \omega \rangle$ in the region near the apex at location c is reduced by a factor of approximately one-half, relative to the peak value at location c for the corresponding stationary wing. Furthermore, in regions approaching the trailing edge of the wing, the vorticity levels for the perturbed wing are generally lower than for those of a stationary wing. At $T_e = 0.75$ s, these lower levels of peak vorticity at c are generally maintained, though at $T_e = 1$ s, the peak at c is slightly elevated. With regard to the clearly identifiable concentrations of vorticity a, they are somewhat disrupted at all values of T_e, though they are generally detectable, especially along the starboard side of the wing.

As shown in Fig. 10, the consequence of the perturbations is generally to increase the peak levels of root-mean-square velocity fluctuation, represented by patterns of v_{rms}/U. The peak values of

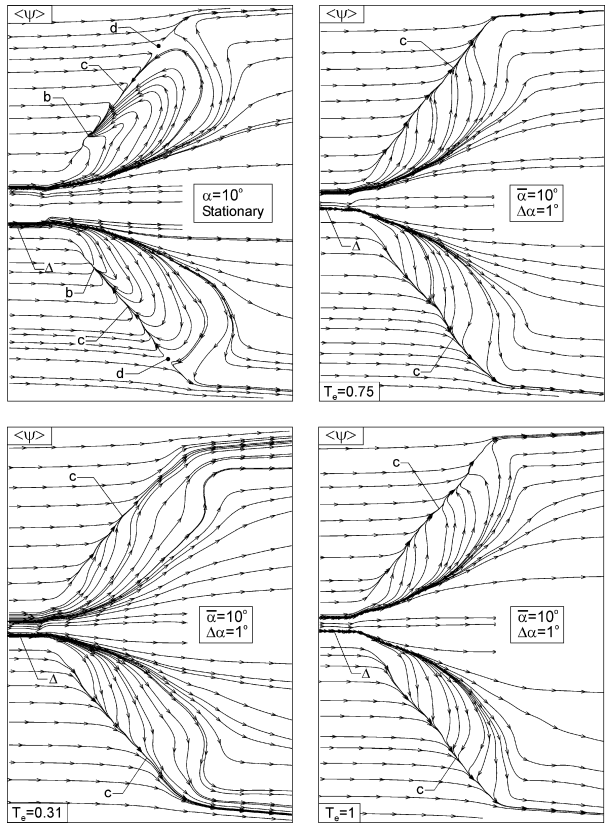

Fig. 8 Patterns of time-averaged streamlines $\langle \Psi \rangle$ on a stationary wing at angle of attack $\alpha = 10$ deg and a wing perturbed according to $\alpha(t) = \bar{\alpha} + \Delta\alpha \sin \omega_e t$, in which $\omega_e = 2\pi/T_e$.

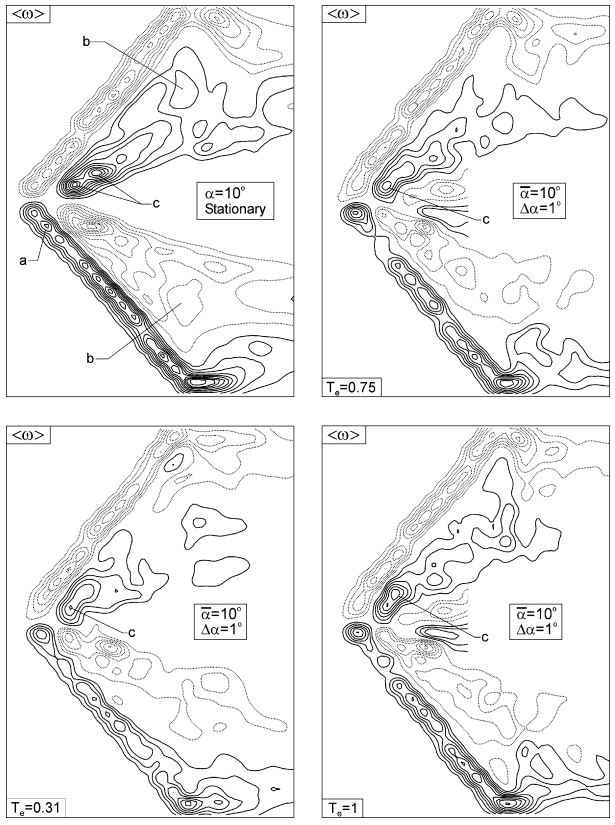

Fig. 9 Patterns of time-averaged vorticity $\langle \omega \rangle$ oriented in a direction normal to the surface of the wing. Stationary wing is at angle of attack $\alpha = 10$ deg, and the perturbed wing is according to $\alpha(t) = \bar{\alpha} + \Delta\alpha \sin \omega_e t$, in which $\omega_e = 2\pi/T_e$; minimum and incremental values are $[|\langle \omega \rangle|]_{\min} = 1\ \text{s}^{-1}$ and $\Delta[|\langle \omega \rangle|] = 1\ \text{s}^{-1}$.

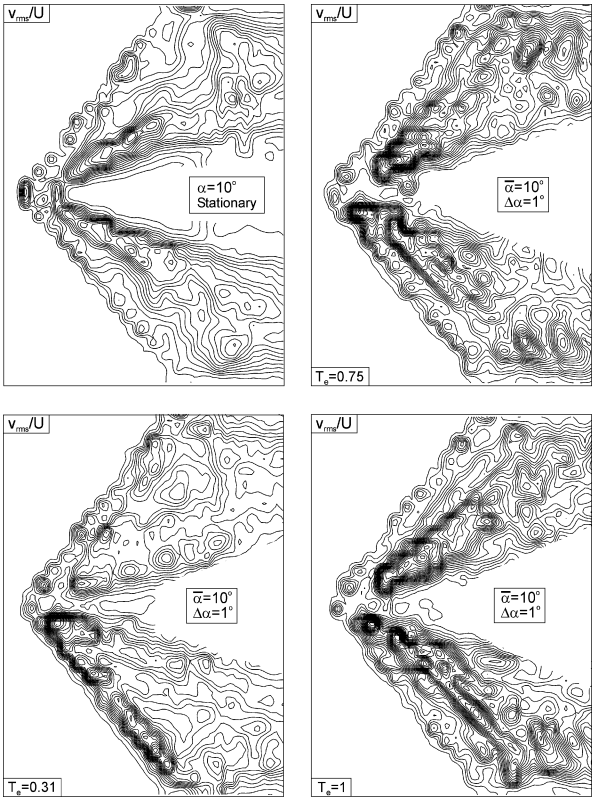

Fig. 10 Patterns of root mean square of transverse velocity fluctuation $v_{\rm rms}/U$ on a stationary wing at angle of attack $\alpha = 10$ deg and a wing perturbed according to $\alpha(t) = \bar{\alpha} + \Delta\alpha \sin \omega_e t$, in which $\omega_e = 2\pi/T_e$; minimum and incremental values are $[v_{\rm rms}/U]_{\rm min} = 0.02$ and $\Delta[v_{\rm rms}/U] = 0.01$.

$v_{\rm rms}/U$ immediately above the surface of the wing can exceed those for the stationary wing by a factor of approximately 1.7. These relatively high levels of $v_{\rm rms}/U$ are evident in the apex region and extend toward the trailing edge.

V. Effect of Transient Motion of Wing on Relaxation of Topology

To determine the relaxation process of the topology to abrupt changes in angle of attack, the wing was pitched from an initial angle $\alpha_i = 3$ deg to a terminal angle $\alpha_f = 10$ deg over a time interval Δt. Two values of $\Delta t = 1$ and 10 s are considered. They correspond to dimensionless ramp rates of $\dot{\alpha}C/2U = 3.6$ and 0.36.

For the highest pitch rate corresponding to $\Delta t = 1$ s, the sequence of topological states is as indicated in Fig. 11. Numbers designated by N^* correspond to increasing values of time t after attainment of the final angle of attack $\alpha_f = 10$ deg. At $N^* = 2$, the value of dimensionless time after cessation of the motion is $tU/C = 0.13$. At successive values of $N^* = 26$, 51, and 151, the corresponding values of tU/C are 1.69, 3.31, and 9.79. At $N^* = 2$, the bifurcation line is designated as c. No saddle and nodal points are detectable. At $N^* = 26$, the direction of the bifurcation line c is maintained. A saddle point sets in at location d, and a nodal point arises at location b on the port side of the wing but is absent on the starboard side. At $N^* = 51$, saddle points d are clearly evident on both sides of the wing. Moreover, the direction of the bifurcation line c has reversed relative to its orientation at $N^* = 2$ and 26. Furthermore, the initial stage of development of a swirl-type pattern is designated at a. At $N^* = 151$, the locations of the saddle points d are consistent with those at $N^* = 51$, and the process of transformation of the bifurcation line c is complete; it extends over a significant portion of the leading-edge region of the wing. Furthermore, pronounced foci, corresponding to tightly wound streamlines, are evident at locations a. In addition to these features, some nodal points are evident. They are designated as b.

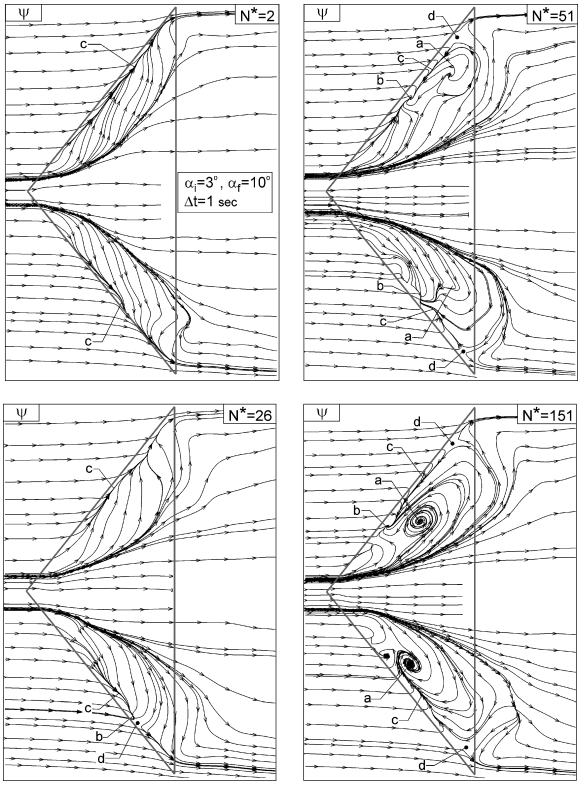

Fig. 11 Patterns of instantaneous streamlines Ψ as a function of frame number N^* after completion of a linear-ramp pitching motion between initial and final angles of attack $\alpha_i = 3$ deg and $\alpha_f = 10$ deg over a time interval $\Delta t = 1$ s corresponding to $U\Delta t/C = 0.972$, in which U is the freestream velocity and C is the wing chord.

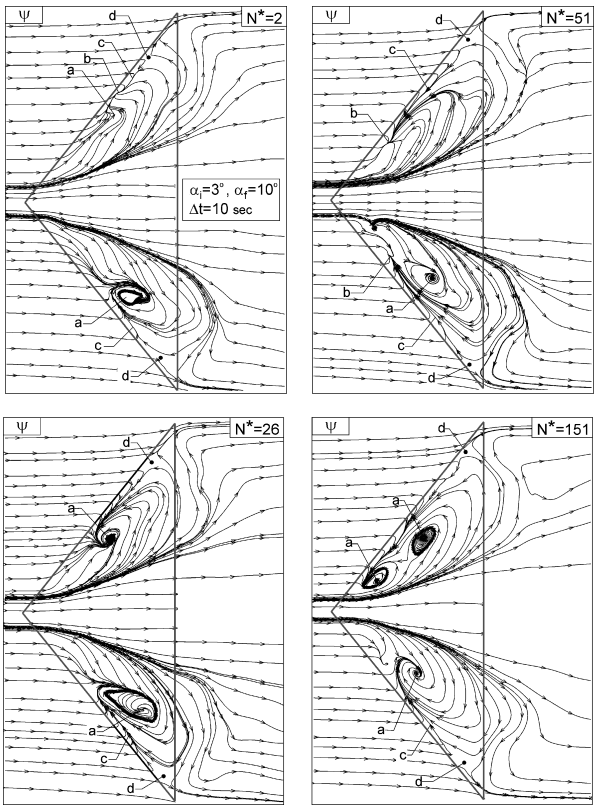

Fig. 12 Patterns of instantaneous streamlines Ψ as a function of frame number N^* after completion of a linear-ramp pitching motion between initial and final angles of attack $\alpha_i = 3$ deg and $\alpha_f = 10$ deg over a time interval $\Delta t = 10$ s corresponding to $U\Delta t/C = 9.72$, in which U is the freestream velocity and C is the wing chord.

For the lower ramp rate, corresponding to $\Delta t = 10$ s, represented in Fig. 12, saddle points *d* are immediately evident on cessation of the wing motion when it reaches its final angle of attack $\alpha = 10$ deg. (See image $N^* = 2$.) These saddle points persist for all subsequent values of N^*. Furthermore, the bifurcation line is oriented toward the apex of the wing at locations *c* for all values of N^*. A predominant feature of all of the patterns is the occurrence of well-defined foci *a* and nodal points *b* in nearly all four parts of Fig. 12.

In the foregoing, emphasis has been on identification of representative critical points of the instantaneous streamline topology of Fig. 12, as well as that of the preceding Figs. 4 and 11; all possible critical points are not designated. In some cases, it is more difficult to assess such points in instantaneous topology, relative to averaged topology, due to the lack of smoothing that is inherent in time averaging. For example, it was pointed out by a referee that an additional saddle point may exist in Figs. 4 ($N^* = 93$), 11 ($N^* = 151$), and 12 ($N^* = 151$). It would be located on the port side of the wing, near the bifurcation line, immediately upstream of the focus *a*. In addition, a potential saddle point is located adjacent to the node *b* on the starboard side of the wing in Fig. 11 ($N^* = 151$). Further assessment of Figs. 4, 11, and 12 involving reinterrogation with a subgrid scheme, and application of spatial filtering, would allow a clearer definition of all additional critical points.

VI. Conclusions

A laser-based technique can effectively provide patterns of instantaneous and averaged flow structure on a plane immediately adjacent to a wing surface, as well as extensions of these patterns to regions upstream of the leading edges and downstream of the trailing edge of the wing. This approach can lead to representations of near-surface streamlines, corresponding patterns of contours of constant streamwise and transverse velocity, and vorticity normal to the surface. The focus of the present investigation is on a delta wing having low sweep angle and sufficiently high angle of attack, such that regions of vortex breakdown occur above its surface. The foregoing representations are provided for the case of the stationary wing, as well as for the wing subjected to small-amplitude perturbations and transient motion in the form of a linear ramp from an initial to final angle of attack. The principal findings are described hereafter.

For the case of the stationary wing, the time-averaged patterns of streamline topology show well-defined critical points, which are symmetrical with respect to the plane of symmetry of the wing. The patterns of instantaneous topology, however, can vary dramatically and contain critical points not evident in the averaged topology. Patterns of time-averaged, surface-normal vorticity effectively complement the time-averaged streamline topology. Vorticity representations are essential for a more complete interpretation of the flow patterns, that is, concentrations of vorticity are not evident in either the instantaneous or time-averaged patterns of the streamline topology. The unsteady aspects of the near-surface fluctuations are evident in corresponding patterns of root-mean-square velocity fluctuation, especially in regions beneath vortex breakdown. This unsteadiness can be further evaluated via space–time (cinema) image acquisition and processing, which leads to evaluation of spectra of the velocity fluctuations at a large number of points over the field of view. With this approach, it is demonstrated that the dimensionless frequencies of vortex breakdown are consistent with the range of frequencies of surface pressure fluctuations computed numerically by Gordnier and Visbal[4] and of velocity fluctuations determined experimentally in a crossflow plane by Yaniktepe and Rockwell.[3]

Perturbations of the delta wing in the pitching mode, in the form of a small angular (pitching) amplitude, can lead to substantial modifications of the time-averaged near-surface topology and velocity fields, at least when the angle of attack of the perturbed wing is coincident with the nominal, steady angle of attack. These alterations are demonstrated in terms of streamline topology and the corresponding averaged surface velocity fields. The number of critical points of the topology can be reduced in the presence of perturbations. Furthermore, a significant reduction in the magnitude of the surface-normal vorticity is attainable at certain locations along the wing surface.

When the wing is subjected to transient pitching motion, the instantaneous near-surface topology, observed at successive times after cessation of the wing motion, can exhibit large variations, provided that the motion varies over a relatively short timescale. Certain critical points of the streamline topology are evident only at larger times. On the other hand, when the timescale of the wing motion is much larger, a number of critical points are evident immediately following cessation of the wing motion: saddle points, nodal points, bifurcation lines directed toward the apex of the wing, and distinct foci. This topology is not, however, representative of that occurring on the stationary wing, thereby suggesting relatively long relaxation times.

The relationship between the near-surface streamlines, characterized herein, and the surface shear stress lines has not been pursued. Rather, emphasis has been on global representations of the steady and unsteady flow structure in the near-surface region. If the intent is to establish such a relationship, then account must be taken of the fact that, as Reynolds number increases, surface-normal gradients will increase, thereby imposing more severe demands on the location and thickness of the laser sheet that defines the plane of interest.

Acknowledgments

The support of the U.S. Air Force Office of Scientific Research (AFOSR) under Grant F49620-02-1-0061 (540074) is gratefully acknowledged. This AFOSR program was monitored by John Schmisseur.

References

[1]Ol, M. V., and Gharib, M., "Leading-Edge Vortex Structure of Nonslender Delta Wings at Low Reynolds Number," *AIAA Journal*, Vol. 41, No. 1, 2003, pp. 16–23.

[2]Gursul, I., Taylor, G., and Wooding, C. L., "Vortex Flows over Fixed-Wing Micro Air Vehicles," AIAA Paper 2002-0698, Jan. 2002.

[3]Yaniktepe, B., and Rockwell, D., "Flow Structure on a Delta Wing of Low Sweep Angle," *AIAA Journal* (to be published).

[4]Gordnier, R. E., and Visbal, M. R., "Higher-Order Compact Difference Scheme Applied to the Simulation of a Low Sweep Delta Wing Flow," AIAA Paper 2003-0620, Jan. 2003.

[5]Visbal, M. R., and Gordnier, R. E., "On the Structure of the Shear Layer Emanating from a Swept Leading Edge at Angle of Attack," AIAA Paper 2003-4016, June 2003.

[6]Hunt, J. C. R., Abell, C. J., Petreka, J. A., and Woo, H., "Kinematical Studies of the Flow Around Free or Surface-Mounted Obstacles; Applying Topology to Flow Visualization," *Journal of Fluid Mechanics*, Vol. 86, 1978, pp. 179–200.

[7]Moffatt, H. K., and Tsinober, A., *Topological Fluid Mechanics*, *Proceedings of the IUTAM Symposium*, Cambridge Univ. Press, Cambridge, England, U.K., 1990.

[8]Tobak, M., and Peake, D. J., "Topology of Three-Dimensional Separated Flows," *Annual Review of Fluid Mechanics*, Vol. 14, 1982, pp. 61–85.

[9]Peake, D. J., and Tobak, M., "Three-Dimensional Separation and Reattachment," *High Angle-of-Attack Aerodynamics*, AGARD Lecture Series 121, 1982, pp. 1-1–1-14.

[10]Peake, D. J., and Tobak, M., "Three-Dimensional Flows About Simple Components at Angle-of-Attack," *High Angle-of-Attack Aerodynamics*, AGARD Lecture Series 121, 1982, pp. 1-1–1-56.

[11]Lazos, B., "Surface Topology on the Wheels of a Generic Four-Wheel Landing Gear," *AIAA Journal*, Vol. 40, No. 12, 2002, pp. 2402–2412.

[12]Su, W., Liu, M., and Liu, Z., "Topological Structures of Separated Flows About a Series of Sharp-Edged Delta Wings at Angles-of-Attack up to 90°," *Topological Fluid Mechanics*, *Proceedings of the IUTAM Symposium*, Cambridge Univ. Press, Cambridge, England, U.K., 1990, pp. 395–407.

[13]Perry, A. E., and Fairly, B., "Critical Points in Flow Patterns," *Advanced Geophysics*, Vol. B14, 1974, pp. 299–315.

[14]Squire, L. C., "The Motion of a Thin Oil Sheet Under the Boundary Layer on a Body," AGARDOgraph 70, 1962.

[15]Lighthill, M. J., *Laminar Boundary Layers*, edited by L. Rosenhead II, Clarendon, Oxford, 1963, pp. 62–82.

[16]Riley, A. J., and Lowson, M. V., "Development of a Three-Dimensional Free Shear Layer," *Journal of Fluid Mechanics*, Vol. 369, 1988, pp. 49–89.

[17]Menke, M., Yang, H., and Gursul, I., "Experiments on the Unsteady Nature of Vortex Breakdown over Delta Wings," *Experiments in Fluids*, Vol. 27, 1999, pp. 262–272.

A. Plotkin
Associate Editor